



## Unravelling the Pleistocene glacial history of the Pamir mountains, Central Asia

Konstanze Stübner <sup>b,\*</sup>, Bodo Bookhagen <sup>a</sup>, Silke Merchel <sup>b,c</sup>, Johannes Lachner <sup>b,c</sup>, Mustafa Gadoev <sup>d</sup>

<sup>a</sup> Institut für Geowissenschaften, Universität Potsdam, Germany

<sup>b</sup> Beschleuniger-Massenspektrometrie und Isotopenforschung, Helmholtz-Zentrum Dresden-Rossendorf, Dresden, Germany

<sup>c</sup> Isotope Physics, University of Vienna, Austria

<sup>d</sup> Institute of Geology, Earthquake Engineering and Seismology, National Academy of Sciences, Dushanbe, Tajikistan



### ARTICLE INFO

#### Article history:

Received 2 November 2020

Received in revised form

10 February 2021

Accepted 16 February 2021

Available online xxx

Handling Editor: C. O'Cofaigh

#### Keywords:

Pleistocene

Quaternary

Glaciation

Central Asia

Cosmogenic isotopes

Geomorphology

Glacial

### ABSTRACT

Several hundred thousand year old moraines preserved in the semi-arid environment of High Mountain Asia attest to Middle Pleistocene glaciations, but the regional correlation of glacial stages and the spatial extent of the glacial advances remain poorly constrained. We examined glacial landforms and Quaternary sediments in the Bartang valley, northwestern Pamir, a region with no previous quantitative glacial chronology. Using cosmogenic  $^{10}\text{Be}$  exposure ages, we dated glacially polished bedrock, moraines, and mass wasting deposits. Our data show that the northwestern Pamir was heavily glaciated in the Middle Pleistocene ( $\geq 220$  ky) with large valley glaciers occupying some of the major valleys in the western Pamir. During the penultimate glacial cycle (191–130 ky) these valleys may have been largely ice free. Catastrophic mega debris flows with volumes  $\geq 0.05 \text{ km}^3$  occurred after the ice retreat and reflect paraglacial destabilization of glacial sediments. The age of the best-dated mega debris flow ( $81 \pm 4$  ky) is similar to moraine ages ~70–80 ky documented throughout the Pamir, demonstrating that remobilized sediments may provide valuable age constraints on glacial histories. In order to facilitate regional comparison of glacial chronologies, we developed a Gaussian separation algorithm, which determines a moraine age from a distribution of boulder exposure ages based on the assumption that post-depositional processes prevail over inheritance, and that the oldest boulder ages best represent the timing of moraine formation. We compiled moraine boulder exposure ages from the Pamir and adjacent regions and provide a summary of Middle and early Late Pleistocene glacial cycles of western High-Mountain Asia.

© 2021 Elsevier Ltd. All rights reserved.

### 1. Introduction

High Mountain Asia contains the highest concentration of glaciers outside of the polar regions (Yao et al., 2012). The monsoon-influenced eastern and southern margins of High Mountain Asia mostly record glacial advances  $\leq 30$  ky, older glacial landforms are preserved in the semi-arid orogenic interior (Amidon et al., 2013; Owen and Dorch, 2014). Quantifying the age and extent of old glacial stages is challenging because in degraded moraines, cosmogenic exposure ages of boulders underestimate the age of moraine formation (e.g. Heyman et al., 2011). Moreover, glacial

sediments may be similar to mass wasting deposits, and distinguishing landslides and rock avalanches from moraines is difficult if the diagnostic morphologies are poorly preserved (Hewitt, 1999; Benn and Owen, 2002). Middle and Late Pleistocene glacial advances in High Mountain Asia have been related to global climate oscillations, to changes in the strengths of regional climate systems, and to topographic controls (e.g., Derbyshire, 1996; Benn and Owen, 1998; Amidon et al., 2013; Dorch et al., 2013). However, the interpretation and regional correlation of glacial stages depend on accurate determination of moraine ages, which is often compromised by highly dispersed boulder ages.

A long history of Pleistocene glacial advances has been documented in the Pamir mountains at the western end of High Mountain Asia (Fig. 1A). The western Pamir is a high-relief mountain range with peak altitudes ~7000 m above sea level (asl) and

\* Corresponding author.

E-mail address: [kstueb@gmail.com](mailto:kstueb@gmail.com) (K. Stübner).

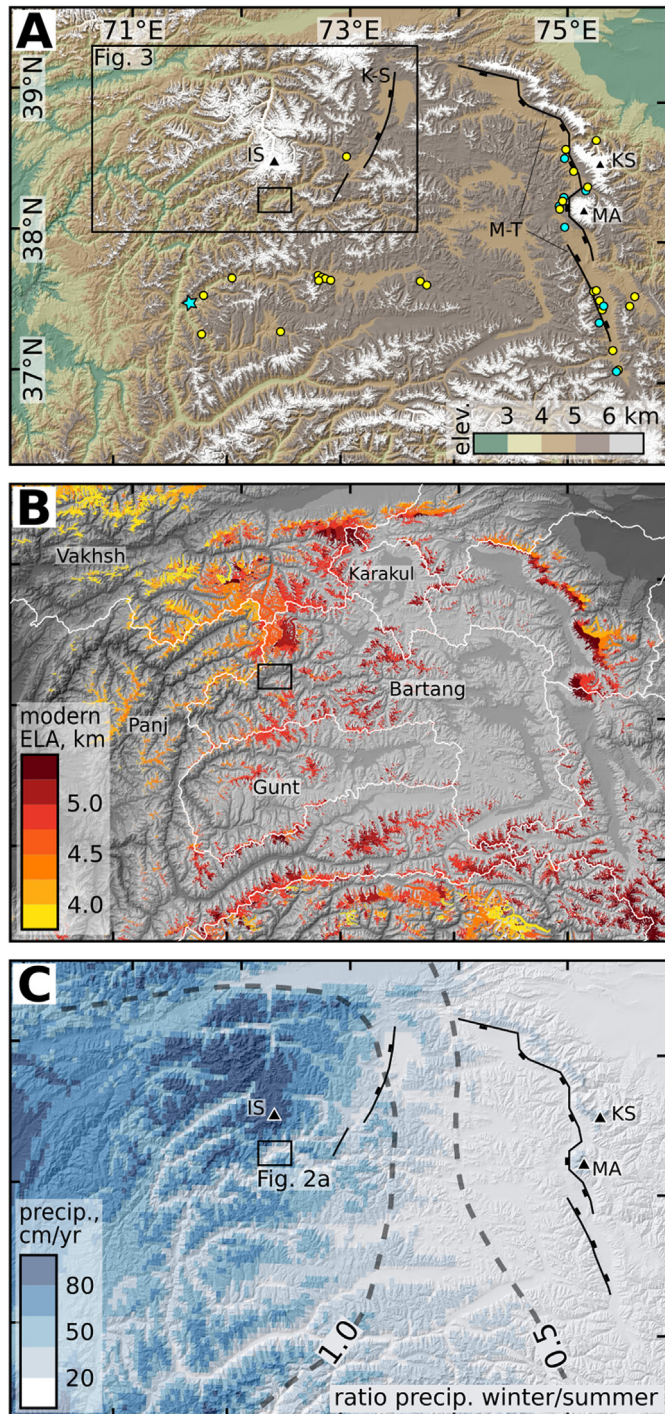


**Fig. 1.** (a) Topography (30 m-resolution SRTM) and glaciers of the Pamir mountains. Dots show locations of previous moraine age studies (yellow: last glacial cycle; blue: penultimate glacial cycle and older). Blue star indicates a roche moutonnée with a penultimate exposure age (see text for references). Rectangles outline study area (**Figs. 2A**) and **Fig. 3**. Abbreviations: K–S: Karakul–Sarez transtensional fault; M–T: Muji–Tashkurgan graben system; IS: peak Ismoil Somoni (7495 m); KS: Kongur Shan (7649 m), MA: Muztagh Ata (7456 m). (b) Equilibrium line altitudes (ELA) of modern glaciers (RGI Consortium, 2017). White lines outline major catchments. (c) Modern annual precipitation and winter-to-summer precipitation ratios (Hijmans et al., 2005). (For interpretation of the references to colour in this figure legend, the reader is referred to the Web version of this article.)

deeply incised valleys (~1500–2500 masl). Glacier snowlines (equilibrium-line altitude, ELA, from the Randolph Glacier Inventory, RGI Consortium, 2017) range from <4000 masl west of the NW Pamir massif to >5000 masl east of the massif (**Fig. 1B**). The ELA variation reflects moisture availability: the Pamir receives precipitation from the mid-latitude westerlies resulting in higher annual precipitation and wetter winters in the western Pamir compared to the east (**Fig. 1C**). An orogenic plateau (median elevation 4350 masl) exists east of ~73°E. The peaks of the “Chinese” Pamir east of the plateau are part of the uplifted footwall of the Muji–Tashkurgan graben system and include the Kongur Shan and Muztagh Ata ice caps (**Fig. 1A–B**). Pleistocene glacial records have been studied in the Chinese Pamir (Seong et al., 2009; Owen et al., 2012; Hedrick et al., 2017), in the central Pamir (Zech et al., 2005; Abramowski et al., 2006; Röhringer et al., 2012) and in the SW Pamir (Stübner et al., 2017, **Fig. 1A**). Despite the abundance of moraine boulder ages, the spatial extent and temporal correlation of glacial advances across the Pamir remain elusive. Here, we provide new age constraints on glacial landforms and mass wasting deposits in the NW Pamir, a region with no previous quantitative glacial chronology. We document extensive Middle Pleistocene valley glaciation consistent with similar results from the SW Pamir (Stübner et al., 2017) and with Middle Pleistocene glacial sediments in the Chinese Pamir (Seong et al., 2009; Owen et al., 2012). To facilitate the regional comparison of Pleistocene glacial chronologies, we developed an algorithm that determines probable moraine ages from dispersed boulder exposure ages based on the assumption that post-depositional processes prevail over cosmogenic nuclide inheritance, and that the oldest boulder ages best represent moraine formation.

## 2. Methods

### 2.1. Field mapping and $^{10}\text{Be}$ dating

We mapped Quaternary deposits and landforms in the upper Bartang valley, NW Pamir (**Figs. 1A** and **2A**). Quaternary deposits were characterized in the field and by the analysis of Google Earth images and 12-m TanDEM-X WorldDEM (Wessel et al., 2018) digital elevation data. We outlined deposits based on their morphology, characteristic colours, and weathering patterns. Special emphasis was put on evidence for erosion of the surface of the deposits such as the development of desert pavement, hillslope hollows and incision, and variability in the weathering of surface clasts. The sediments were investigated in fresh outcrops exposed through stream incision or recent slope failure; we noted grain sizes and grain size distribution, lithological composition, sorting, stratification and clast morphology. However, many deposits lack fresh exposure, or freshly exposed cliffs are inaccessible, and for some of the deposits we can only provide a first-order sedimentological characterizations.

To constrain the age of Quaternary deposits, we sampled boulder and bedrock surfaces for cosmogenic  $^{10}\text{Be}$  exposure age dating during September and October 2017. For each sampled boulder, we recorded boulder size and evidence of surface weathering and potential boulder relocation. Topographic shielding was recorded in the field for each sample locality. Samples were processed at the University of Potsdam following the methods described in Von Blanckenburg et al. (2004) and Merchel et al. (2019). After crushing and sieving, quartz was concentrated using standard mineral separation techniques and chemical cleaning with  $\text{HCl}/\text{H}_2\text{SiF}_6$  followed by chemical cleaning with HF (1–2 wt%). For each sample ~20 g purified quartz were dissolved after adding ~300 µg of a low-ratio  $^9\text{Be}$  carrier ( $^{10}\text{Be}/^{9}\text{Be}$  ratio of  $1.62 \times 10^{-16}$ ). Beryllium was separated by ion-exchange chromatography; a

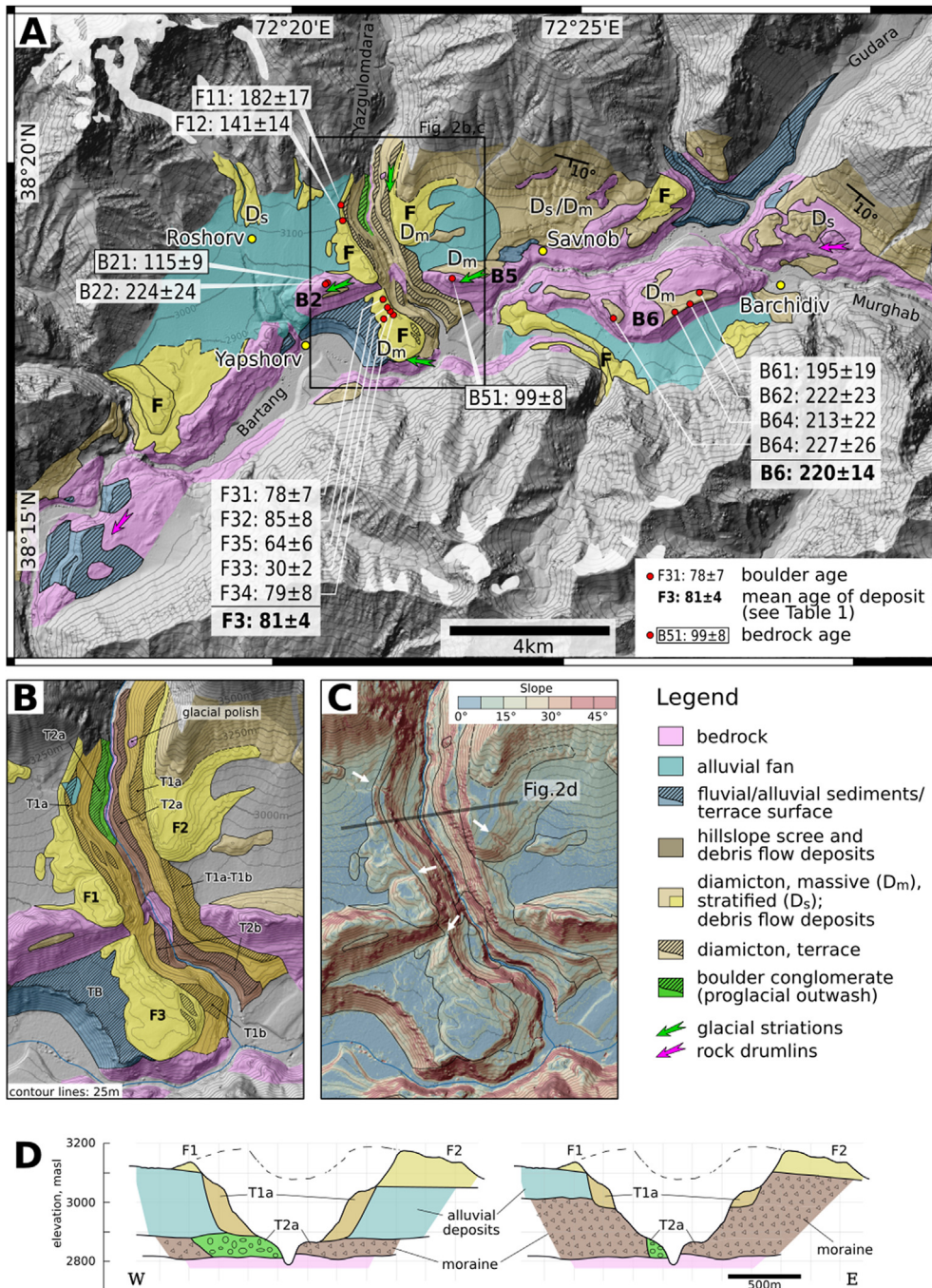


**Fig. 2.** (a) Quaternary geologic map of the upper Bartang basin and new  $^{10}\text{Be}$  exposure ages. Bedrock ages showing glacial polish are calculated assuming 0 mm/ky erosion; boulder ages assuming 1 mm/ky. F1 to B6 denote the landforms (F: debris-flow deposits; B: bedrock hillocks) targeted for  $^{10}\text{Be}$  dating. Diamictic deposits interpreted as mega debris flows are highlighted yellow (see Discussion). (b) Detailed map of the lower Yazgulomdara valley showing river terraces and interpreted mega debris-flow deposits (F1, F2, F3). Terraces are labelled according to their relative age (upper/older: T1; lower/younger: T2) and their position (a: upstream; b: downstream of the axial bedrock ridge). TB: Bartang river terrace. Note the deeply incised bedrock gorge downstream of the Bartang–Yazgulomdara confluence. (c) Shaded relief and hillslopes calculated from 12 m-resolution TanDEM-X WorldDEM digital elevation data (Wessel et al., 2018), same area as Fig. 2b. White arrows highlight erosional features on the surface of the flow deposits. Location of cross section (Fig. 2d) is indicated. (d) Cross sections of the Yazgulomdara terrace system. Left and right panel show different possible interpretations (see section 3.2). (For interpretation of the references to colour in this figure legend, the reader is referred to the Web version of this article.)

detailed description of our laboratory procedures is provided in the Supplement (Text DR1).  $^{10}\text{Be}/^{9}\text{Be}$  ratios were measured by Accelerator Mass Spectrometry at the Vienna Environmental Research Accelerator (VERA; Steier et al., 2019). Exposure ages were calculated with the CronusEarth calculator v 2.0 (Marrero et al., 2016) using spallation production rates of Borchers et al. (2016) and the  $^{10}\text{Be}$  half-life of Korschinek et al. (2010). Table 1 summarizes ages

calculated with the time-variable Lal/Stone scaling scheme, a sea level–high latitude  $^{10}\text{Be}$  production rate of  $4.00 \pm 0.32$  atoms/g/y, and erosion rates of 0 and 1 mm/ky; analytical data and age results calculated with other available scaling schemes are provided in the Supplement Table DR2.

**Table 1**Sample locations and  $^{10}\text{Be}$  exposure age dates.

Sample	Latitude (°N)	Longitude (°E)	Elevation (m asl.)	Boulder height (cm)	Lithology	Comment	Exposure age, 0 mm/ky <sup>a</sup> (ky)	Exposure age, 1 mm/ky <sup>a</sup> (ky)
<b>Diamicton F1</b>								
F11	38.326	72.349	3133	95	conglomerate schist	strongly fractured	155 ± 14	182 ± 17
F12	38.322	72.350	3131	170	staurolite schist	fractured, maybe tilted	125 ± 10	141 ± 14
<b>Hillock B2</b>								
B21 <sup>b</sup>	38.308	72.346	3198		quartz vein in slate	fractured bedrock surface	115.3 ± 9.2	
B22	38.308	72.346	3198	45	slate		187 ± 14	224 ± 24
<b>Diamicton F3</b>								
F31	38.305	72.362	2913	70	gneiss	concave erosion forms on the side	78.4 ± 7.0 <sup>c</sup>	84.5 ± 7.9 <sup>c</sup>
F32	38.303	72.363	2885	60	granite		74.3 ± 6.5 <sup>c</sup>	79.7 ± 7.8 <sup>c</sup>
F33	38.302	72.364	2896	200	gneiss		29.6 ± 2.3	30.3 ± 2.4
F34	38.301	72.365	2894	200	gneiss	strong wind erosion in lower half	73.6 ± 6.4 <sup>c</sup>	78.8 ± 7.6 <sup>c</sup>
F35	38.301	72.362	2831	140	gneiss		60.9 ± 5.0	64.2 ± 5.5
							weighted average of oldest boulders:	
							75.3 ± 3.8	80.9 ± 4.5
<b>Hillock B5</b>								
B51 <sup>b</sup>	38.310	72.382	3077		quartzitic slate	glacially polished bedrock	98.8 ± 7.8	
<b>Diamicton on top of hillock B6</b>								
B61	38.308	72.453	3165	100	granite	fractured, maybe tilted; surface dip dir/dip: 160/55	156 ± 14	195 ± 19
B62	38.306	72.450	3202	145	granite	strong concave wind erosion forms	186 ± 14 <sup>c</sup>	222 ± 23 <sup>c</sup>
B63	38.304	72.447	3249	90	granite		180 ± 15 <sup>c</sup>	213 ± 22 <sup>c</sup>
B64	38.302	72.428	3267	150	granite	wind erosion on the side	188 ± 14 <sup>c</sup>	227 ± 26 <sup>c</sup>
							weighted average of oldest boulders:	
							184.8 ± 8.3	220 ± 14

<sup>a</sup> Lal/Nishiizumi time-dependent scaling scheme, SLHL production rate  $4.00 \pm 0.32$  atoms/g/y. Uncertainty includes  $^{10}\text{Be}$  production rate uncertainties.<sup>b</sup> Bedrock surface; all other samples are from boulders.<sup>c</sup> Included in the calculation of the weighted average of the oldest boulders.

## 2.2. Boulder age statistics and moraine ages

Calculated  $^{10}\text{Be}$  exposure ages depend on the used scaling scheme and production rate, and the surface erosion rate, which is in most cases unknown. To integrate our new data with previously published exposure dates and facilitate a regional comparison of glacial chronologies in western High Mountain Asia, we recalculated earlier published  $^{10}\text{Be}$  data with parameters used for our age calculations (time-variable Lal/Stone scaling, SLHL production rate  $(4.00 \pm 0.32)$  atoms/g/y, erosion rates 0 mm/ky and 1 mm/ky; [Supplement Table DR3](#)). The effects of scaling and erosion rate on the nominal  $^{10}\text{Be}$  age become more significant with increasing age, and for samples  $\geq 100$  ky different scaling schemes predict ages that may vary by several tens of percent (e.g., [Owen and Dorch, 2014](#)). The effects of inaccurately estimated surface erosion rates may be even more severe (c.f. [Table 1](#)), making it virtually impossible to compare  $^{10}\text{Be}$  exposure ages  $\geq 100$  ky with independently determined timelines such as isotopic climate records (see [Balco, 2011](#)).

In addition to these challenges in calculating accurate  $^{10}\text{Be}$  exposure ages, the determination of a moraine age from boulder ages and thus the regional comparison of moraine ages and glacial chronologies is hampered by a variety of geological processes such as boulder toppling, moraine degradation and post-depositional shielding, or inheritance of cosmogenic nuclides at the time of boulder deposition, which result in boulder ages that are younger or older than moraine formation, respectively (e.g., [Applegate et al., 2010](#)). Different methods have been proposed to deal with this scatter from chi-squared statistics and different outlier-determination schemes to numerical models that predict components of degradation and inheritance in boulder age distributions (see review in [Balco, 2011](#)). Some moraine age studies in High Mountain Asia rely on the mean of all boulder ages or the mean age after excluding some young or old outliers (e.g., [Owen et al., 2012](#);

[Röhringer et al., 2012](#)). Other authors assert that most boulder ages are too young and infer the moraine age either from the oldest boulder (e.g., [Abramowski et al., 2006](#); [Zech et al., 2013](#)) or the mean of several of the oldest boulders (e.g., [Seong et al., 2009](#)). [Chevalier et al. \(2011\)](#) interpret the outlier-corrected mean and the oldest boulder ages as minimum and maximum estimate for the moraine age, respectively. Especially for the older moraines dated in these studies ( $>40$  ky), young boulder ages that are inconsistent with the inferred stratigraphic age are common and are dismissed in favour of older boulder ages ([Owen et al., 2002, 2006, 2012](#); [Zech et al., 2005, 2013](#); [Abramowski et al., 2006](#); [Seong et al., 2007, 2009](#); [Dorch et al., 2010](#); [Hedrick et al., 2011, 2017](#); [Zech, 2012](#); [Stübner et al., 2017](#)). Regional comparison of these data thus requires not only the recalculation of  $^{10}\text{Be}$  exposure ages but also a uniform approach to obtain a moraine age from boulder age data.

To this end, we developed a Gaussian separation approach inspired by a similar method proposed by [Dorch et al. \(2013\)](#). The approach is based on the assumption that post-depositional effects resulting in incomplete exposure prevail over inheritance (e.g., [Heyman et al., 2011](#)), and that the oldest boulders of a moraine best represent moraine formation. First, we grouped the recalculated  $^{10}\text{Be}$  boulder ages by moraine or group of moraines of similar ages following the suggestions of the original authors ([Supplement Table DR3](#)). For each group of boulder ages, we compute a Kernel Density Estimation (KDE) with an optimized bandwidth that reflects the number and spread of boulder ages. Then we separate the KDE into Gaussian curves (Gaussian Mixture Model). The number of Gaussian curves  $n$  is determined by iteratively increasing  $n$  until the misfit between the KDE and the Gaussian Mixture Model defined as area percent of the KDE is  $<1\%$ . We report the location, width and area (in percent of the Gaussian Mixture Model) of each Gaussian; the location of the oldest peak with an area  $>5\%$  is interpreted as the probable moraine age. The width of the peak and the area

indicate, how well this moraine age is constrained by the data; a small area or a wide peak may suggest a low quality of the resulting moraine age. The algorithm does not test whether the oldest peak is statistically significant, and the predicted moraine ages should not be used without inspection of the graphical output of the program. Boulder ages that are interpreted as inheritance ages, e.g., based on stratigraphic constraints, should be excluded from the input data prior to KDE smooting. For the purpose of this study, we report recalculated moraine ages with an uncertainty of 10%. A detailed description of the algorithm and the code written in python are provided (Supplement Text DR1 and [https://github.com/kstueb/MoraineAge\\_GaussianMixture](https://github.com/kstueb/MoraineAge_GaussianMixture)).

### 3. Results

#### 3.1. Landforms of the upper Bartang valley

The Bartang river valley is one of the narrowest and most deeply incised valleys of the western Pamir. The topographic relief calculated over a 10-km radius is 3–4 km, valley cross sections are V-shaped, and the valley floor is typically not much wider than the river channel (50–100 m). East of 72°15'E, the valley widens to form the ~5 × 20 km<sup>2</sup> upper Bartang basin (Fig. 2A). The basin is connected to the glaciers of the NW Pamir massif via the 75 km long and ~1 km wide Tanymas–Gudara valley, a putative Pleistocene glacial valley (Zabirov, 1955; Abramowski et al., 2006, Fig. 3).

A flat-topped, several kilometres wide bedrock ridge with peak elevations ~3000 to 3300 masl runs along the centre of the basin (Figs. 2A and 4A). Bedrock flats near the towns of Savnob and Barchidiv and at the western end of the basin feature a knobby surface with elongated, several hundred metres long and up to 50-m-high rock hummocks oriented in a E-W to NE-SW direction (Fig. 4C); surface elevations of the bedrock flats are ~2700–2900 masl. The bedrock—Upper Triassic dark slate—is covered by a thin veneer of weathered rock. We documented glacial polish in several locations on the bedrock ridge and on lower-elevation bedrock flats (Figs. 2A and 4D).

Locally, the river has incised into the bedrock forming up to 200-

m-deep, narrow gorges; in other reaches, the bed widens to a braided stream (Fig. 4B). River terraces up to 250 m above river level exist in the centre and at the western end of the basin. The terraces consist of horizontally stratified sequences of reddish-brown conglomerate, matrix-supported silty conglomerate, and intercalated silt layers. Clasts are rounded to subrounded and range in size from coarse sand to cobbles and boulders. The terrace sediments are mostly poorly sorted and dominated by matrix-rich layers (Fig. 4E–F).

In the eastern (upper) part of the basin, tens of metres to >100 m of diamictic deposits overlie bedrock flats near Savnob and Barchidiv and the large bedrock hillock B6. Near Savnob, the diamicton is exposed from 2700 to 3300 masl and is overlain by hillslope deposits consisting of scree and debris-flow deposits that dip 5–10° towards the basin centre (Figs. 2A and 4G,I). The surface of the deposit is strongly degraded, and fresh exposure is scarce. The diamicton is massive to horizontally stratified with angular to subrounded, mixed-lithology clasts (slate, schist, granite) ranging in size from <1 cm to ~1 m in a grey silty matrix; boulders >1 m are rare. The deposits appear to form two or more terraces (e.g., at 2950 and 3200 masl; Fig. 4I). Small cliffs west of Savnob expose fluvial reddish conglomerate deposited on top of the bedrock. The conglomerate is overlain by silt. The total thickness of the sequence is ~100 m, and its top is level with the upper tread of the large Bartang river terrace 3 km farther west (Fig. 2A). The depositional relationship between the conglomerate–silt sequence and the diamicton could not be established.

Near Barchidiv, incision of the Murghab river exposes ~150-m-thick diamicton deposited on top of bedrock flats (Fig. 4J). Similar to the exposure around Savnob, the bedrock surface is at 2800–2900 masl, and the top of the diamicton is between 3100 and 3250 masl and overlain by hillslope scree and debris flows dipping ~10° towards the valley centre. The diamicton shows subhorizontal stratification, and an angular unconformity separates the diamicton from the overlying hillslope deposits.

The diamicton on the bedrock hillock B6 fills depressions, drapes over summits, and forms a 60-m-high ridge along the southern margin of the hillock. The surface of the deposit is

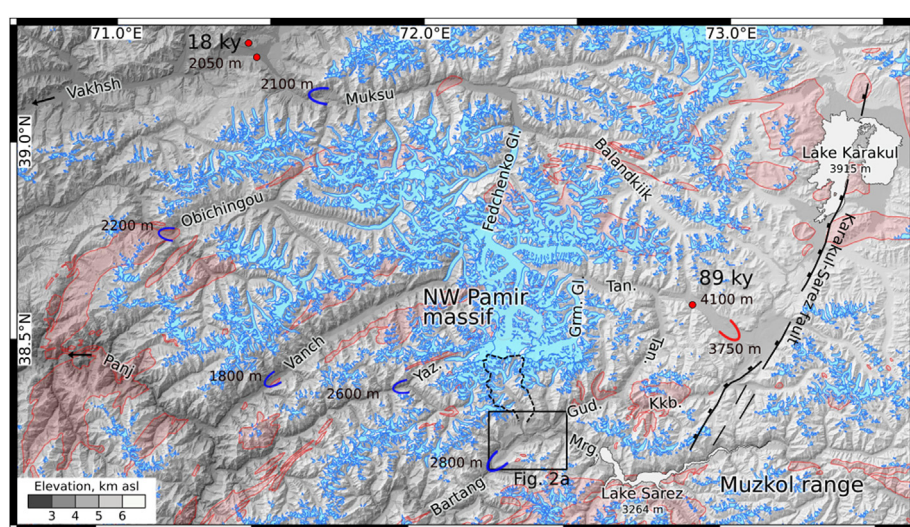


**Fig. 3.** Topography and glaciers of the NW Pamir. The largest glaciers are the 77-km-long Fedchenko glacier and the 25-km-long Grumm-Grzhimaylo glacier (Grm. Gl.). Red shading outlines exposure of granitic and granodioritic rocks (after Vlasov et al., 1991). In the eastern part of the map, a half-graben extends from Lake Karakul to Lake Sarez. Valleys that are mentioned in the text are labelled (Tan.: Tanymas, Gud.: Gudara, Kkb.: Kokubel, Mrg.: Murghab valley). Blue markers indicate our minimum estimates of the extent of the Bartang stage glaciation (see Discussion). Red markers show locations of ~18 ky lateral and recessional moraines of the Fedchenko–Muksu glacier (Grin et al., 2016) and Late Pleistocene moraines (~89 ky; Abramowski et al., 2006) and proposed maximum eastern extent of the Pleistocene Tanymas glacier (Zabirov, 1955). Outlines of Fig. 2A and the Yazgulomdara river catchment are indicated. (For interpretation of the references to colour in this figure legend, the reader is referred to the Web version of this article.)

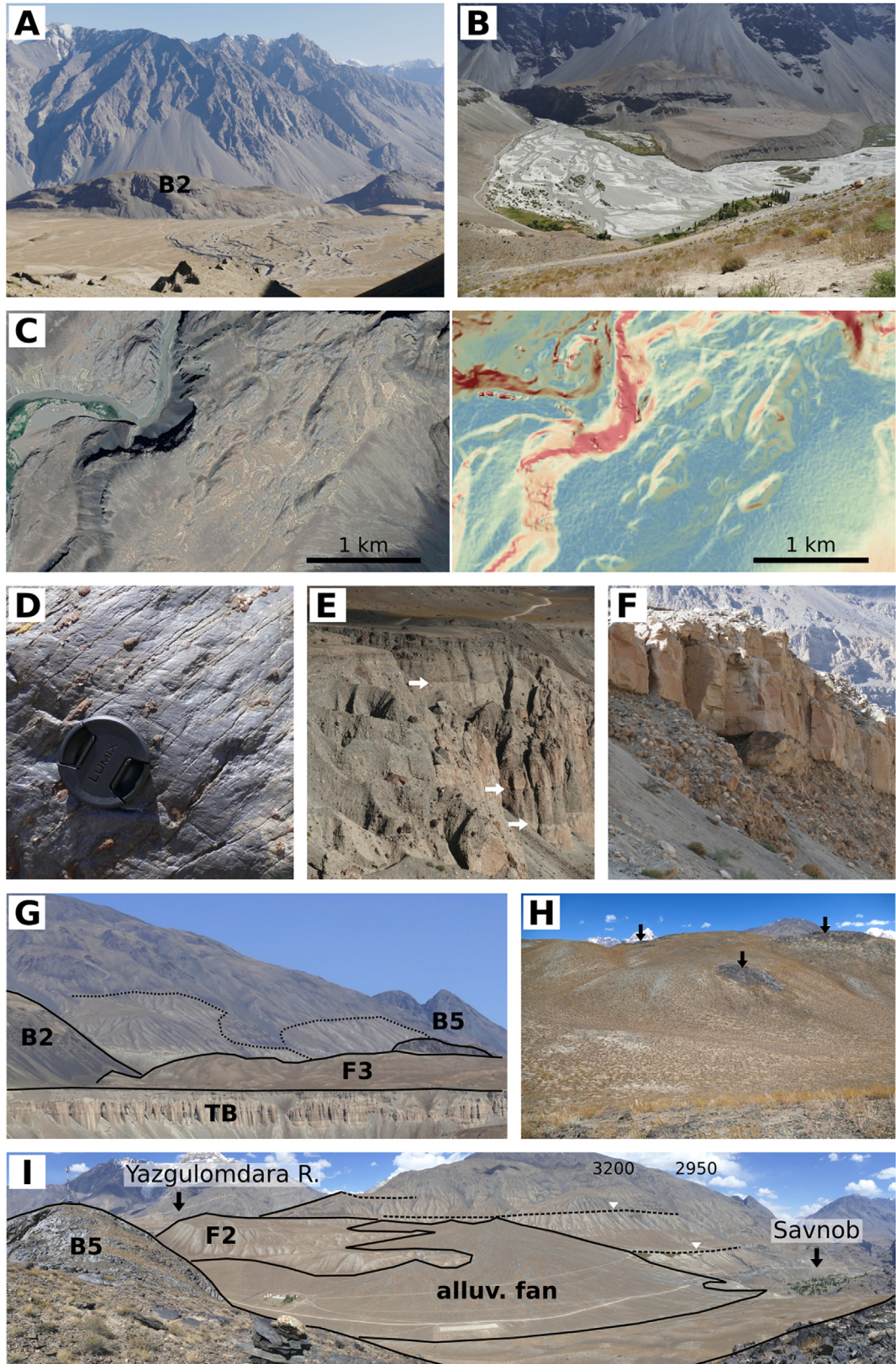


**Fig. 4.** (a) View down the Roshorv alluvial fan onto the axial bedrock ridge in the upper Bartang basin. Photo location and view direction are shown in Fig. 3Q. (b) View upstream the Bartang river. Braided stream and river terraces in the foreground, narrow, 150-m deep bedrock gorge in the background. (c) Google Earth image (left) and slope map (right; see Fig. 2D for legend) of the rock hummocks on bedrock flats at the western end of the basin. (d) Glacially polished Triassic slate from the top of bedrock hillock B5 (Sample location B51). (e) Sequence of stratified, silt-rich conglomerates with intercalated silt layers and lenses of the Bartang river terrace; arrows highlight layering. Outcrop is ca. 100 m high. (f) Conglomerate overlain by silt layer at the top of the Bartang river terrace. Outcrop is ~5 m high. (g) Field photo of the bedrock hillock B2 and debris-flow deposit F3 overlying the Bartang river terrace TB. In the background, on the other side of the Yazgulomdara river, the diamictic deposits north of the town of Savnob are outlined by dashed lines. (h) View of the degraded diamicton covering bedrock hillock B6. Arrows highlight bedrock outcrops. (i) View from bedrock hillock B5 to the north. The diamictic deposits that cover the bedrock

flats near Savnob form several large terraces, e.g., at 2950 and 3200 masl (dashed lines and white triangles). Hillslope deposits at higher elevations are generally darker coloured (see also Fig. 3G). A large alluvial fan overprints the terraced diamictic deposits. (j) View from hillock B6 upstream the Murghab river (marked blue). Dashed lines highlight the contact between bedrock flats and diamictic deposits in the Murghab valley and on top of B6. White triangles mark the top elevations of the diamictic deposits. (k) View from the upper terrace (T1a) down the Yazgulomdara valley. The central bedrock ridge (hillock B2) and the debris-flow deposit F3 behind the ridge are visible in the background. (l) On the left side of the Yazgulomdara river, terrace T2a consists of massive diamicton overlying bedrock. The river is visible in the lower part of the photo. Field of view is ca. 80 m high. (m) On the right side of the river, terrace T2a exposes boulder conglomerate. (n) Well-stratified, matrix-rich coarse sand and conglomerate succession that crops out in the northern part of terrace T2a, and which contrasts with the massive to weakly stratified diamicton of terrace. (o) View of the terrace T1a on the left side of the river overlain by deposit F2. Arrows highlight indistinct layering of the diamicton that is locally visible. (p) View up the Yazgulomdara valley. The diamictic deposit F1 forms a distinct ridge that rises 10 m above the alluvial fan, al, and 50 m above the terrace, T1a. Pink arrow marks glacially polished bedrock that crops out in the riser of the upper terrace. Blue arrow marks an erosional gap within the ridge that connects the Roshorv alluvial fan with conglomeratic outcrops within the terrace T1a (see Fig. 2C). (q) Detail of Fig. 2A showing the locations and view directions of landscape photos in Fig. 4 (left) and outcrop locations (right). (For interpretation of the references to colour in this figure legend, the reader is referred to the Web version of this article.)

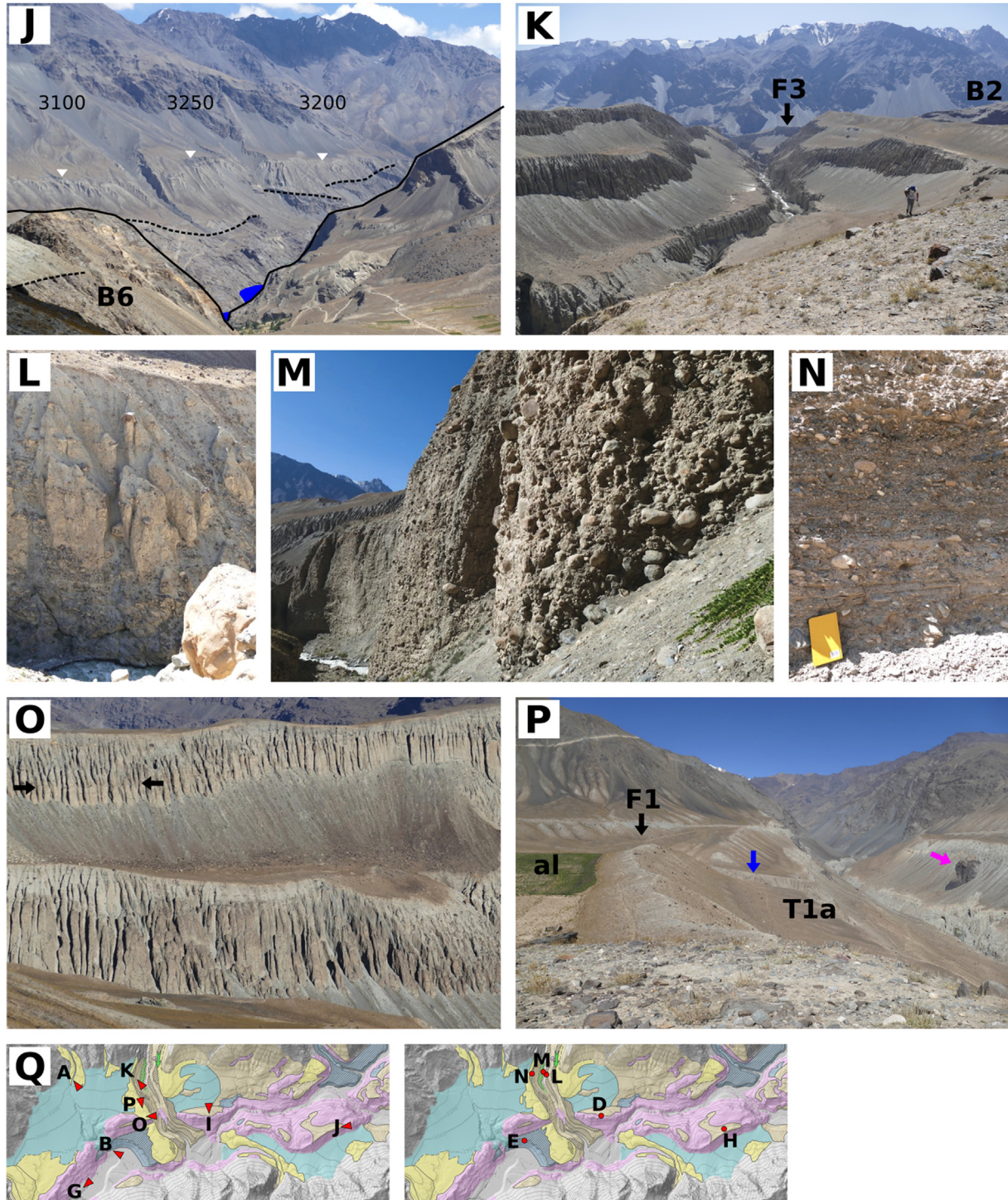


Fig. 4. (continued).

strongly degraded with hillslope hollows and shallow alluvial depressions; the underlying bedrock is locally exposed (Fig. 4H). Fresh sediment exposure is limited to the cliff along the southern margin. The clast sizes, lithologies and angularities of the diamicton are similar to the deposits near Savnob, stratification was not documented. Local hilltops of the diamicton are covered by desert pavement, and there are several large (1–2 m) granite boulders.

North and south of the axial bedrock ridge are large alluvial fans 400 m above the river level. The “Roshorv” alluvial fan is deeply incised by the Yazgulomdara river, a glaciated catchment north of the basin (Fig. 2A–C). From its entry into the basin to the confluence with the Bartang river, the Yazgulomdara river is flanked by two pairs of terraces ~100 m and ~250 m above river level (Fig. 2B and C, 4K). Upstream from the bedrock ridge, the river is a bedrock channel incising black slate. On the left side of the river, the bedrock is overlain by massive diamicton with angular, up to 1 to 2-m-large blocks (Fig. 4L). On the right side of the river, the terrace T2a exposes massive, poorly sorted, clast-supported boulder conglomerate with rounded clasts ≤1 m in a silty-sandy matrix (Fig. 4M). Clasts comprise sandstone, slate, schist and, more rarely, limestone, conglomerate and magmatic rocks, consistent with the lithologies exposed in the upper Yazgulomdara catchment.

The upper terraces T1a and both terrace pairs T1b and T2b downstream from the bedrock ridge consist of diamicton with boulders up to 50 cm. On an outcrop scale the diamicton appears massive; weak to well-defined stratification is visible from the distance (Fig. 4O). Stratification is subparallel to the terrace surfaces. Upstream from the bedrock ridge, terrace surfaces and stratification dip ~5–10° in a downstream direction; downstream from the ridge, the dip angles are steeper (~10–15°), and stratification of the diamicton is more clearly defined. Locally, the upper terrace T1a on the river right includes a sequence of well stratified, poorly sorted, clast-supported to matrix-supported fine conglomerate (clasts mostly slate and limestone, 0.5–10 cm) and silty layers and lenses (Fig. 4N; location indicated by blue arrow in Fig. 4P and by blue polygon in Fig. 2B). On the river left, glacially polished bedrock crops out within the upper terrace riser (Fig. 4P, pink arrow).

Above the upper terraces there are large diamictic deposits with a smooth, undulating surface and a lobate outline (Fig. 2B and 2C; F1, F2, F3). The deposit F1 lies on top of the Roshorv alluvial fan. Its northern part is a 10-m-high ridge along the edge of the fan (Fig. 4P), its southern part is up to 80 m thick and laps onto the bedrock hillock B2. The surface slopes gently ( $\leq 15^\circ$ ); the eastern boundary is sharp and dips ~30° towards the Yazgulomdara river. At two locations, the deposit is deeply incised by abandoned channels (white arrows in Fig. 2C). The northern one of these cuts connects the Roshorv alluvial fan with the localised exposure of well stratified conglomerate within the diamictic terrace T1a. Apart from these channels there is little evidence for erosion of the deposit. The sediments of F1 comprise diamicton with angular to subrounded clasts ≤2 m in a light grey silty matrix; clast composition is similar to the stratified diamicton of the Yazgulomdara terraces (i.e., mostly slate and schist, some limestone and conglomerate). Stratification was not observed in F1.

The deposit F3 south of the bedrock ridge is 200 m lower than F1 and has similar characteristics: Surface slopes are  $\leq 15^\circ$ , the western boundary is lobate and abuts a Bartang river terrace (TB), the eastern and southern boundaries dip steeply towards the Yazgulomdara and Bartang rivers. Apart from two small terraces in the southeastern part of the deposit and a small hillslope hollow at its northern end, the surface of the deposits shows little degradation (Fig. 2B–C). The steep cliffs along the northeastern margin of the deposit expose massive, grey diamicton with angular to subrounded slate, schist, gneiss, and granite clasts up to 2 m. Deposits

that are morphologically similar to F1 and F3 exist in other parts of the basin and were mapped based on satellite imagery and TanDEM-X data (Fig. 2A).

### 3.2. Cross sections of the Yazgulomdara terrace system

Glacial polish on bedrock flats and hillocks shows that the upper Bartang basin was glaciated in the past. We interpret the boulder conglomerate in T2a as proglacial outwash. The massive diamicton overlying bedrock on the river left terrace T2a may be residual moraine material. The terraces T2a upstream of the bedrock ridge are strath terraces (Fig. 2B–D). The construction of a complete cross section of the Yazgulomdara terrace system is difficult due to the lack of knowledge of the thickness and stratigraphy of the Roshorv alluvial fan, and due to the incomplete exposure of the terrace risers, the lower part of which are concealed by thick scree deposits (e.g., Fig. 4K). Two possible cross sections are shown in Fig. 2D. The reconstruction of the left side assumes that T1a are ~150 m thick cut-and-fill terraces consisting of alluvial material from the Yazgulomdara catchment. The Roshorv alluvial fan, which the terraces are cut into, may consist mostly of older alluvial material sourced north and east of the basin (Fig. 2D, left). The presence and thickness of moraine material below the Roshorv fan are speculative.

Alternatively, the cut-and-fill terraces T1a may have a much lower thickness, and the lower part of the terrace risers may be part of an older alluvial or glacial sequence preserved below the Roshorv alluvial fan (Fig. 2D, right). The verification of these models requires not only more complete exposure of the terrace sediment sequences, but also the unequivocal distinction between alluvial diamicton and moraine material; the massive to weakly stratified diamicton exposed in T1a is consistent with either interpretation. The terraces T1b and T2b downstream from the bedrock ridge consist of stratified diamictic material, and we interpret them as alluvial deposits.

### 3.3. Exposure age data

Samples from the diamictic deposit F1 are from 95 to 170 cm high, strongly fractured schist boulders (Fig. 5, F11, F12). Only two boulders yielded sufficient quartz for analysis. Because of the poor preservation of these boulders the exposure ages ( $155 \pm 14$  ky and  $182 \pm 17$  ky assuming 0 mm/ky erosion; Table 1) likely underestimate the deposition age. Samples from deposit F3 are from 60 to 200 cm high granite and orthogneiss boulders, some of which have concave erosion forms on the side and in their lower half (Fig. 5, F31–F35). Exposure ages range from  $29.6 \pm 2.3$  to  $78.4 \pm 7.0$  ky (0 mm/ky erosion). Three of five boulders yielded indistinguishable ages with a weighted mean of  $75 \pm 4$  ky; these include the strongly eroded boulders F31 and F34. Four boulders from the diamicton on top of B6 are lithologically and morphologically similar to those of F3 (Fig. 5, B61–B64). Boulder ages range from  $156 \pm 14$  ky to  $188 \pm 14$  ky (0 mm/ky erosion) with a weighted mean of the three oldest boulders of  $185 \pm 8$  ky; these include boulder B62, which has strongly sculpted erosion forms on its side. A 45 cm high slate boulder from bedrock hillock B2 yielded an exposure age of  $187 \pm 14$  ky. Glacially polished bedrock samples B21 and B51 (Figs. 5 and 3D) yielded exposure ages of  $115 \pm 9$  ky and  $99 \pm 8$  ky, respectively.

Assuming an erosion rate of 1 mm/ky yields ~5–25% older boulder ages with weighted mean ages of  $81 \pm 4$  ky for F3 (3 of 5 boulders) and  $220 \pm 14$  ky for B6 (3 of 4 boulders; Table 1). An erosion rate of 3 mm/ky yields a mean of  $95 \pm 6$  ky for F3 whereas boulders from B6 do not yield valid ages (i.e., the measured  $^{10}\text{Be}$  concentrations are higher than the saturation levels). Fig. 2A shows boulder exposure ages calculated with 1 mm/ky erosion and



**Fig. 5.** Boulder and bedrock locations sampled for  $^{10}\text{Be}$  exposure age dating. Sample number are indicated in the top right of each photo.

bedrock exposure ages calculated with 0 mm/ky erosion.

#### 4. Discussion

##### 4.1. Quaternary evolution of the upper Bartang basin

The bedrock morphology in the upper Bartang basin was shaped by glacial erosion (axial ridge, hillocks, bedrock flats) and subsequent fluvial re-equilibration (river gorges, Bartang river terraces). The axial ridge, the glacial striations, and the knobby bedrock, which we interpret as rock drumlins, indicate a W to SW direction of ice flow. The Bartang glacier was probably sourced in the NW

Pamir massif from where it flowed via the Tanymas and Gudara valleys (Fig. 3). The accumulation area may have included the >6000 masl massifs enclosing Lake Sarez east of the basin. This interpretation is supported by bedrock flats overlain by diamictic material in the lower Murghab valley (Fig. 4J) indicative of glacial erosion. Glacial polish on the side of the Yazgulomdara valley shows that the Yazgulomdara glacier formerly extended into the basin. The boulder conglomerate and the massive diamicton in the river terraces T2a may represent some of the oldest glacial and proglacial sediments preserved in the basin.

After deglaciation, the upper Bartang basin was filled with several hundred metres of sediments including glacial and

proglacial sediments and the alluvial fans north and south of the axial bedrock ridge. The deposit F1 overlies, i.e., postdates, the sequence of sediments below the Roshov alluvial fan. The morphology of F1 suggests that it results from catastrophic sediment discharge from the Yazgulomdara catchment. We interpret F1 as an enormous debris-flow deposit with a volume on the order of 0.05–0.08 km<sup>3</sup>; the ridge at the upper end of F1 (Figs. 2B–C, 4P) is interpreted as a lateral levee of the flow. The deposit F2 may be a remnant of the same flow or result from a separate event; F3 postdates F1. The stratified diamicton and the terraces of the lower Yazgulomdara valley (T1b, T2b) result from a prolonged history of channelized debris flows discharged from the Yazgulomdara catchment during progressive incision into the Roshov sediment sequence. The axial bedrock ridge acted as a barrier for the debris flows; it formed a backstop for the mega debris flow F1 and accounts for the change in dip angles of the terraces and the diamictic stratification across the ridge. After the upper terraces T1a and T1b were abandoned, continued incision cut through the bedrock ridge and produced the strath terraces T2a, whereas alluvial terraces T2b were deposited downstream of the ridge. Deposits that are morphologically similar to F1 to F3 show that these mega debris flows were widespread in the upper Bartang basin (Fig. 2A).

Interpretation of the diamicton covering the bedrock flats near Savnob and Barchidiv is ambiguous because of the stronger degradation of these deposits. The lack of a distinct stratification in the diamicton north of Savnob supports an interpretation of these deposits as ancient moraine from the Bartang glacier. The terraced morphology of the deposits (Fig. 4I) may result from fluvial incision into a sequence of dominantly glacial sediments. Alternatively, the 'terraces' may represent remnants of strongly degraded sets of lateral moraines of the Bartang glacier. On the other hand, the stratification in the diamicton north and east of Barchidiv may indicate alluvial deposition resulting from debris flows sourced in the Gudara and Murghab valleys and their tributaries.

The lithologies of the upper Bartang basin and its more proximate catchments comprise Carboniferous to Jurassic sandstone, siltstone and carbonate, and their metamorphic equivalents (Vlasov et al., 1991). The granite boulders on top of the massive B6 diamicton contrast with these lithologies. They may originate from voluminous Cretaceous granite intrusions that are exposed in the Kokuibel valley and around Lake Sarez implying that they have been transported at least 30 km along the Gudara or Murghab valleys. Other potential granitic source areas are located in the northern part of the NW Pamir massif or in the eastern Muzkol range and require transport distances on the order of 100 km (Vlasov et al., 1991, Fig. 3). The transport of these sediments over tens of kilometres, and their deposition on top of a hillock ~200 m above the Savnob and Barchidiv bedrock flats supports an interpretation of the B6 diamicton as Bartang glacier moraine. Based on this argument, we also favour an interpretation of the Savnob and Barchidiv diamicton as glacial deposits. Likewise, the source of the granitic and gneissic boulders from the mega debris flow F3 is not in the Yazgulomdara catchment, and we suggest that F3 consists of recycled moraine of the Bartang glacier.

#### 4.2. Age constraints and the extent of Bartang glacial stage

The age of the mega debris flow F3 is reasonably well constrained by boulder exposure ages (Table 1). We interpret the mean of the oldest boulders as the age of deposition and attribute the younger boulder ages to post-depositional remobilization. The concave erosion forms in the granitic and gneissic boulders in the upper Bartang basin (Fig. 5, e.g., F31–F34, B62, B64) suggest that boulder erosion is significant. A maximum steady-state erosion rate can be estimated from the boulders with the highest <sup>10</sup>Be

concentrations assuming that these are in erosional equilibrium. For boulders B22, B62, B63 and B64 we obtain maximum erosion rates between 2.8 and 2.9 mm/ky comparable to rates of 2.3 mm/ky reported for the Chinese Pamir (Owen et al., 2012). Although boulder erosion rates up to 3–5 mm/ky have been employed in other parts of the Pamir (Zech et al., 2005; Abramowski et al., 2006; Röhringer et al., 2012), we propose that a rate of 1 mm/ky is more appropriate (see also Seong et al., 2009). Assuming an erosion rate of 1 mm/ky, the age of deposition of F3 is 81 ± 4 ky; the no-erosion age of 75 ± 4 ky is a minimum deposition age (Table 1). The older boulder ages of F1 compared to F3 are consistent with the relative ages of the mega debris flows, and we interpret the oldest boulder (F11: 182 ± 17 ky; all ages are quoted for 1 mm/ky erosion unless specified otherwise) as the minimum age of this deposit.

The last glaciation of the upper Bartang basin predates the debris flows and is thus at least Middle Pleistocene; we refer this glacial stage as the Bartang stage. The polished bedrock samples (B21: 115 ± 9 ky; B51: 99 ± 8 ky; both ages 0 mm/ky erosion) likely underestimate deglaciation if the central bedrock ridge was covered by sediments. The retreat of the Bartang glacier is constrained by boulders from the B6 diamicton (mean age B6: 220 ± 14 ky), which we interpret as Bartang stage moraine. This interpretation is consistent with the ages of the debris flows, the polished bedrock samples and a boulder from the bedrock ridge (B22: 224 ± 24 ky). The glacial and proglacial sediments exposed in terrace T2a are not dated but predate deposition of the Roshov alluvial fan, deposition of the mega debris flows F3 and F1, and development of the Yazgulomdara terrace system, and we tentatively attribute them to the Bartang stage.

Because moraines are not preserved in the Bartang valley the Pleistocene glacial chronology remains poorly constrained. The Bartang stage ended at ~220 ky; subsequent glacial advances may have reached the basin, but there is no evidence for glaciation of the upper Bartang basin in the last 220 ky. The ice extent during the Bartang stage can be estimated from first-order ELA approximations. The toe-to-headwall altitude ratio (THAR) approach assumes that the ELA lies at a fixed proportion of the vertical distance between the highest and lowest limits of the glacier (Benn and Lehmkuhl, 2000). With THAR = 0.5 and assuming constant headwall elevations, the ELA difference ( $\Delta$ ELA) between modern and Bartang-stage glaciers can be estimated as  $0.5 \cdot (A_0 - A_B)$ , where  $A_0$  and  $A_B$  are the toe elevations of modern glaciers and the Bartang valley glacier, respectively. The lowest-elevation outcrops of glacially polished bedrock at the western end of the upper Bartang basin are at 2800 masl; with toe elevations of modern valley glaciers in the upper Tanymas valley of 3600–4000 masl (e.g., Grumm-Grzhimaylo glacier; Fig. 3)  $\Delta$ ELA is on the order of 400–600 m. Using a conservative estimate of  $\Delta$ ELA = 400 m, the THAR approach suggests that during the Bartang stage the major valleys in the NW Pamir were glaciated at least down to elevations between 1800 and 2600 masl. The corresponding palaeo-glacier toes are indicated in Fig. 3 and show that major NW Pamir valleys were completely (e.g., Muksu, Balandkiik, Tanymas, Gudara valleys) or largely (Obichingou, Vanch valleys) glaciated in the past. We consider this reconstruction a minimum estimate of the Bartang stage ice extent not only because  $\Delta$ ELA = 400 m is a conservative estimate but also because we cannot exclude the possibility that the Middle Pleistocene Bartang glacier reached beyond the western end of the upper Bartang basin.

The length of the Fedchenko–Muksu glacier during the global Last Glacial Maximum is constrained by ~18 ky recessional and lateral moraines near the confluence of the Muksu and Vakhsh valleys (Grin et al., 2016, Fig. 3). There is general agreement that glacial advances in the Pamir and Tian Shan during the global Last Glacial Maximum were considerably less extensive than earlier

Pleistocene advances (e.g., Seong et al., 2009; Owen et al., 2012; Röhringer et al., 2012; Zech, 2012, this study), and these moraines confirm that the glacier toes outlined in Fig. 3 truly underestimate the extent of the Bartang stage glaciation. We suggest that in the NW Pamir, several glaciers attained lengths of >100 km during the Middle Pleistocene Bartang glacial stage, and that the Fedchenko–Muksu and Vanch glaciers most likely extended into the Vakhsh and Panj valleys, respectively.

On the east side of the NW Pamir massif, a subsidiary tongue of the Tanymas glacier flowed eastwards towards the Karakul–Sarez half-graben. Zabirov (1955) argues that the maximum Pleistocene extent of this tongue ended just short of the half-graben (Fig. 3, glacier tongue marked in red). The suggested toe elevation of 3750 masl is almost 1000 m higher than implied by the THAR estimation of the extent of the Bartang glaciation (e.g., compared to the toe elevation of 2800 masl of the Bartang glacier). This discrepancy might be attributed to different ages of the reconstructed ice extent; the Tanymas glacier toe shown in Fig. 3 is undated and may represent a less extensive glacial advance postdating the Bartang stage. On the other hand, present-day ELAs east of the NW Pamir massif are hundreds of metres higher than those north and west of the massif (Fig. 1B), and it is, therefore, plausible that the proposed eastern toe of the Tanymas glacier does belong to the Bartang glacial stage. Poorly preserved lateral moraines 13 km northwest to the toe, which have been dated ~89 ka (Abramowski et al., 2006; recalculated age, see Fig. 6, B12), suggest that the eastern tongue of the Tanymas glacier existed in the Late Pleistocene but do not constrain its extent during the Bartang stage. Therefore, it remains unclear to what extent the Karakul–Sarez half-graben was glaciated in the past.

#### 4.3. Glacial chronologies of western High Mountain Asia

To compare the age constraints from the upper Bartang basin with regional glacial chronologies, we re-evaluated  $^{10}\text{Be}$  moraine age data compiled from the literature using a dedicated Gaussian separation algorithm to explore the density function of boulder ages. Erosion rates of 3 mm/ky are inconsistent with the  $^{10}\text{Be}$  concentrations determined in many of the oldest samples, and we interpret ages calculated with erosion rates of 0 and 1 mm/ky as minimum and best estimates, respectively (Supplement Table DR3). Fig. 6 illustrates the reanalyses for Marine Isotope Stage (MIS) 5 moraines in the north-central, south-central and in the Chinese Pamir (all ages are quoted for 1 mm/ky erosion). For data sets with a relatively narrow, unimodal age distribution the reanalysed moraine age is similar to the arithmetic mean of boulder ages (Fig. 6 age group B33). In other data sets, the algorithm identifies the oldest peak in the age distribution as the probable moraine age (Fig. 6, age groups B42, B32, and C32). Some of the boulder age distributions have a distinct youngest age peak between ~20 and ~40 ky, and we speculate that some of the young peaks in moraine boulder data may represent a time period of intensified moraine reworking, e.g., due to a wetter climate. The potential to use our algorithm to explore episodic boulder remobilization is not further explored here.

The blue bars in Fig. 6 indicate moraine age interpretations by the original authors but based on recalculated boulder ages; for B32 this is the oldest boulder age, for all other age groups it is the mean of a subset of boulder ages (Zech et al., 2005; Abramowski et al., 2006; Owen et al., 2012; Röhringer et al., 2012; Hedrick et al., 2017). In general, the Gaussian separation of KDE-smoothed age distributions yields moraine ages that are in agreement with the

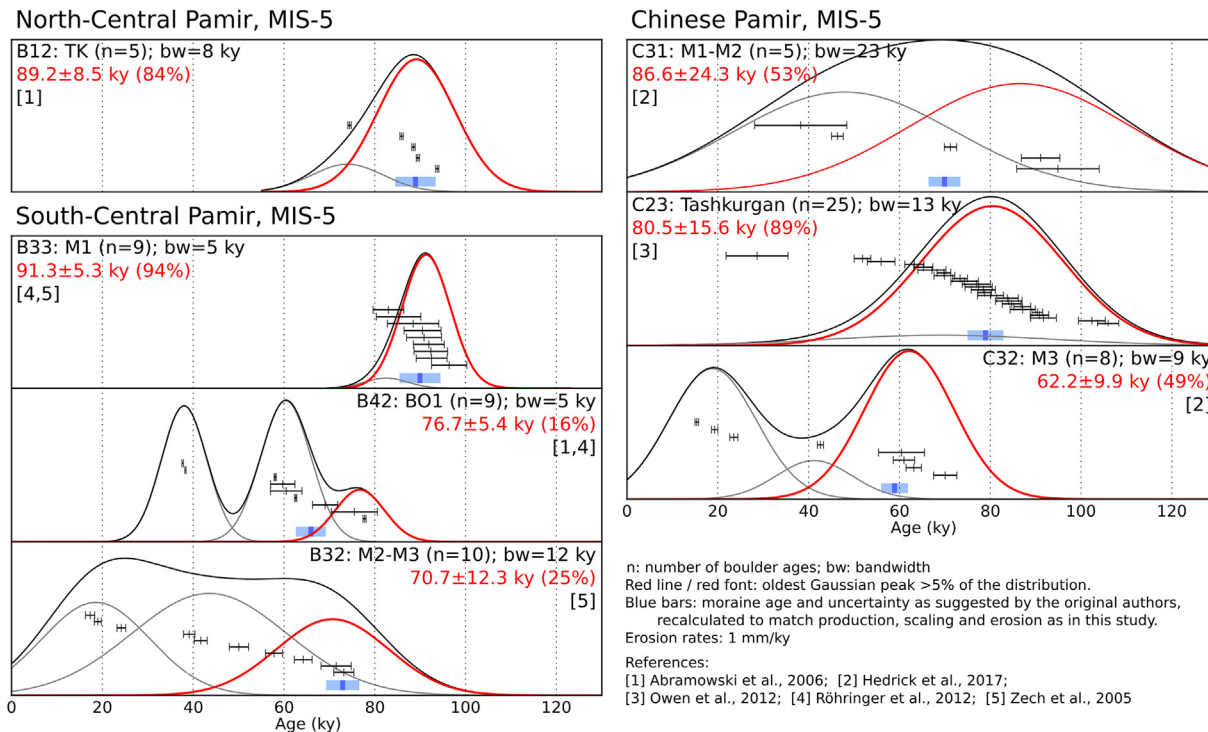


**Fig. 6.** Moraine boulder  $^{10}\text{Be}$  ages from the literature and results of our Gaussian separation algorithm exemplified for MIS-5 moraines from the north-central and south-central (left) and the Chinese Pamir (right). Blue bars indicate the age and uncertainty of the moraines as proposed by the original authors but recalculated to match production rates, scaling and erosion rates used in this study. References are shown in each panel. See Supplement Figure DR5 for similar diagrams for all moraines of our literature data compilation. (For interpretation of the references to colour in this figure legend, the reader is referred to the Web version of this article.)

original interpretations while it eliminates the need to manually select outliers; for highly dispersed data sets, our reanalysed ages differ from the original ages by as much as 20% (Fig. 6; B42, C31). The algorithm provides the means to explore boulder age distributions, but it does not test the statistical significance of age peaks, and it is up to the user to assess the reliability of a suggested moraine age (for example, see the poorly defined peaks of C31, C23 in Fig. 6). We generally interpret the moraine ages as minimum estimates because (a) for highly dispersed boulder ages it is not known whether any of the boulder ages represent the true age of moraine formation (e.g., Fig. 6, B32, B42), and (b) for unimodal age distributions the mean may be much smaller than the oldest boulder ages (e.g., Fig. 6, C23).

Suggested (minimum) moraine ages from the Tian Shan, Pamir, Chinese Pamir, Karakoram, Ladakh and West Tibet are summarized in Figs. 7 and 8; moraines younger than the global Last Glacial Maximum are excluded from this analysis. Although there is considerable uncertainty and dispersion in the results, some first-order features are evident: Most dated moraines are <100 ky corresponding to the last glacial cycle (MIS-5d to MIS-2). Older moraines (MIS-6 and older) are rare but have been documented in most parts of western High Mountain Asia suggesting that the documented age distribution represents a sampling and moraine preservation bias and that Middle Pleistocene glacial advances may have been widespread.

There is some clustering of Middle Pleistocene moraine ages for data sets across different regions, but the absolute ages are uncertain. For example, moraines in the Chinese Pamir ('Dabudaer' stage of Owen et al., 2012) and Ladakh suggest a glacial maximum at ~300 ky if boulder erosion rates of 1 mm/ky are assumed (Fig. 8), whereas erosion rates between 0 and 2 mm/ky yield ages between

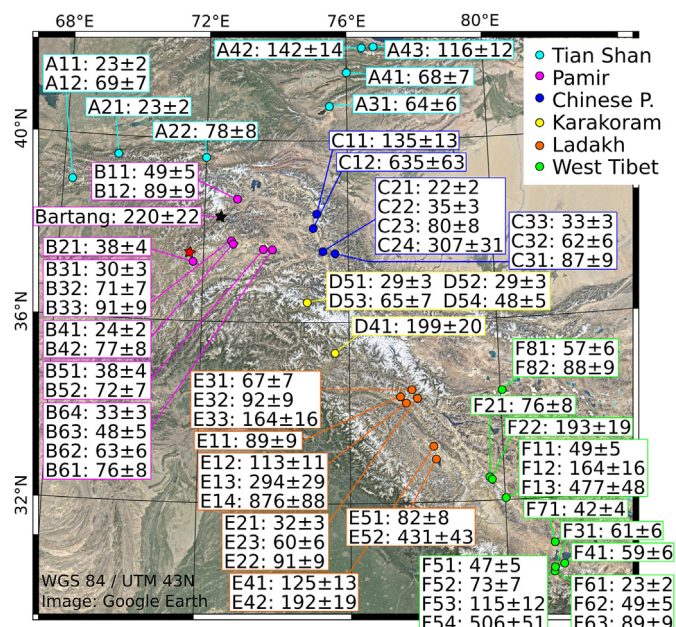


**Fig. 7.** Interpreted moraine ages in the Tian Shan, Pamir, Chinese Pamir, Karakoram, Ladakh, and West Tibet (based on compilation by Owen and Dorch, 2014, with additions from Amidon et al., 2013; Hedrick et al., 2017; Stübnér et al., 2017) assuming boulder erosion rates of 1 mm/ky. Raw data, computational results, and a similar figure for 0 mm/ky erosion are provided in the Supplement (Tables DR3, DR4; Figures DR5, DR6). Figure figs1 Labels 'A11' to 'F82' correspond to the grouping of boulder ages (see Tables DR3, DR4). Black star indicates this study; red star indicates  $142 \pm 10$  ky roche moutonnée in the Gunt valley (Stübnér et al., 2017). All moraine ages are shown with 10% uncertainty. (For interpretation of the references to colour in this figure legend, the reader is referred to the Web version of this article.)

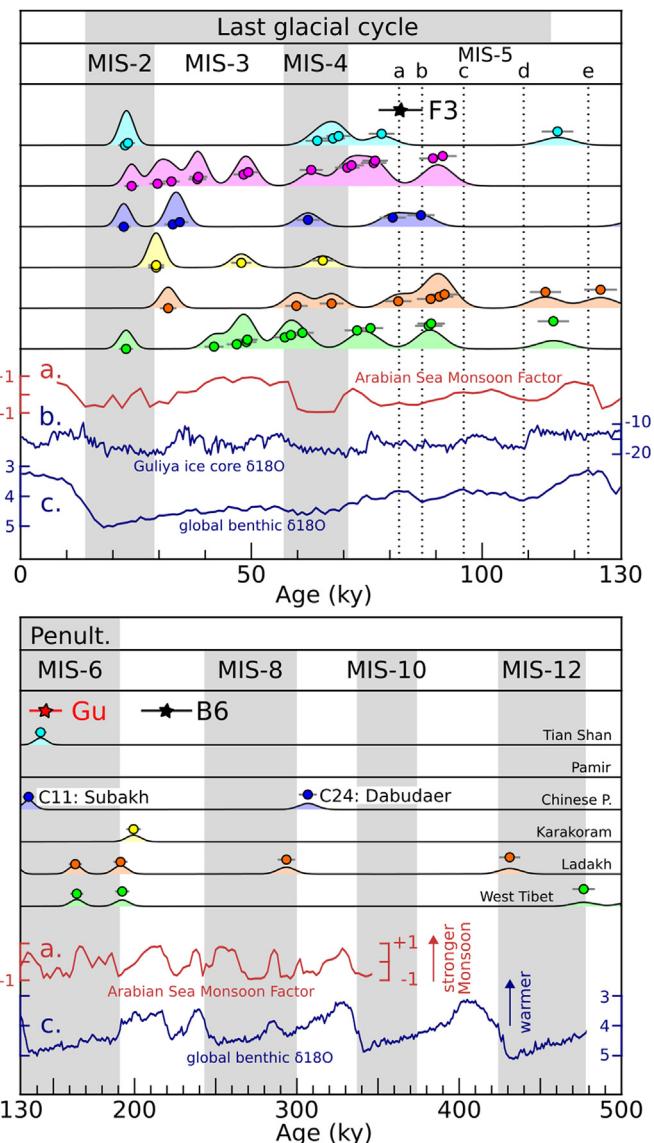


**Fig. 8.** Age distributions of the moraine ages shown in Fig. 7. Black and red stars: ages of the mega débris flow F3, the diamictite B6, and a  $142 \pm 10$  ky roche moutonnée in the Gunt valley ('Gu'; Stübnér et al., 2017). 'C11: Subakh' and 'C24: Dabudaer': Middle Pleistocene glacial stages in the Chinese Pamir (Seong et al., 2009; Owen et al., 2012). Climate proxy curves show a: Arabian Sea Monsoon Factor (Clemens and Prell, 2003); b: Guliya ice core  $\delta^{18}\text{O}$  (Thompson et al., 1997); c: global benthic  $\delta^{18}\text{O}$  (Lisiecki and Raymo, 2005). Marine isotope stages (MIS) and MIS peaks 5a to 5e after Lisiecki and Raymo (2005). Note the change in x-axis scaling at the Middle-to-Late Pleistocene boundary. (For interpretation of the references to colour in this figure legend, the reader is referred to the Web version of this article.)

~200 ky and ~550 ky. This uncertainty prohibits a meaningful discussion about climatic controls such as the strength of the summer monsoon or global temperature on the Middle Pleistocene glacial stages. The age of the diamictite B6 in the upper Bartang basin is MIS-7. Although moraines with similar ages have been documented in the Karakoram, Ladakh, and West Tibet the correlation of Middle Pleistocene moraines is only tentative (Fig. 8). It is, however, clear that the glacial advance that shaped the upper Bartang basin predates the penultimate glacial cycle (MIS-6).

In the Chinese Pamir, the Middle Pleistocene 'Karasu' glacial stage is represented by >150 m thick glacial sediments in the centre of the Muji–Tashkurgan valley (Seong et al., 2009, Fig. 7: C12). Its age is poorly constrained by five boulder ages ranging from 180 to

635 ky. Subdued, hummocky moraine fields of the 'Subakh' glacial stage in the Chinese Pamir have previously been attributed to the Late Pleistocene (MIS-3 to MIS-4; Seong et al., 2009). Although our re-evaluation suggests an older moraine age of ~135 ky (Fig. 7: C11; Fig. 8; see also Dorch et al., 2013), the Subakh stage postdates the Bartang glacier. Farther south in the Tashkurgan valley, the Middle Pleistocene 'Dabudaer' stage is represented by highly eroded moraine remnants (Owen et al., 2012); our re-evaluation suggests an age of ~310 ky (Fig. 7: C24; Fig. 8). Although our Gaussian separation algorithm yields distinct ages for the Karasu and Dabudaer stages, the suggested age of the Karasu stage is based on a single boulder age >600 ky, and we cannot rule out the possibility that these stages are, in fact, a single Middle Pleistocene glacial stage. Both the Karasu and Dabudaer glacial stages are older than the Bartang stage.

Stübner et al. (2017) argue for extensive Middle Pleistocene valley glaciation in the SW Pamir based on roche moutonnée exposure ages from the Gunt valley (recalculated  $142 \pm 10$  ky; 'Gu' in Fig. 8). Because of sediment cover on many of the SW Pamir roches moutonnées this age likely underestimates the time of deglaciation. Although these data allow for the possibility of a penultimate age of the Gunt glacier, we propose that the most widespread glaciation of the Pamir occurred in one or several Middle Pleistocene advances before MIS-6 (Karasu and Dabudaer stage(s), Bartang and Gunt glaciers); during the penultimate glacial cycle the major valleys of the western Pamir may have been largely ice free.

Late Pleistocene moraine ages are less sensitive to the boulder erosion rates. There is some clustering of moraine ages around MIS-5b (~90 ky), especially in the Pamir, Ladakh, and West Tibet (Fig. 8, top panel; see also Fig. 6). MIS-4 moraines are widespread throughout western High Mountain Asia and correspond to a global temperature low, documented in  $\delta^{18}\text{O}$  signals from benthic sediments (Lisiecki and Raymo, 2005) and the Guliya ice core (Thompson et al., 1997), but also to a weakened summer monsoon (Clemens and Prell, 2003, Fig. 8). The oldest moraines documented in the south-central Pamir and on the Pamir plateau formed during MIS-4 and late MIS-5 (~63–91 ky; Abramowski et al., 2006; Röhringer et al., 2012). Numerous MIS-3 moraines have been documented in the Pamir and in West Tibet whereas fewer such records exist in other parts of western High Mountain Asia (Fig. 8).

We correlate the mega debris flow F3 ( $81 \pm 4$  ky) to a global warm period at MIS-5a and speculate that rising temperatures resulted in glacial melting, paraglacial destabilization of older moraine material, and deposition of the mega debris flows in the NW Pamir. Moraine ages ~70–80 ky have been reported from the Pamir (e.g., Fig. 6: B42, B32), Chinese Pamir, and other parts of western High Mountain Asia (Figs. 7 and 8). Tentative regional correlation of these moraines suggests that widespread deglaciation may have occurred between MIS-5a and the beginning of MIS-4, i.e., during a global interglacial. Glacial advances in High Mountain Asia are limited by precipitation and may reflect the strength of the mid-latitude westerlies and the Indian summer monsoon circulation patterns rather than global temperature (e.g., Benn and Owen, 1998; Owen and Dorch, 2014; Batbaatar et al., 2018). The ~70–80 ky moraines in the Pamir may thus result from glacial retreat due to weakening of the mid-latitude westerlies and increasing aridity in the Pamir. Following this line of argument, the paraglacial destabilization that led to deposition of the mega debris flow F3 may be driven by aridization of the Pamir rather than rising temperatures.

## 5. Conclusions

We documented glacial erosion surfaces and glacial, proglacial

and paraglacial sediments in the upper Bartang valley, NW Pamir. Using cosmogenic  $^{10}\text{Be}$  exposure ages of boulders and glacially polished bedrock, we constrained the Middle and Late Pleistocene glacial history and landscape evolution:

- In the Middle Pleistocene, the Tanymas–Gudara–Bartang glacier extended over >100 km from the NW Pamir massif to the upper Bartang basin. The 'Bartang' glacial stage ended at ~220 ky. We propose that the largest Bartang stage glaciers in the NW Pamir extended down to elevations  $\leq 1800$  masl, and probably resulted in partial glaciation of the Vakhsh and Panj valleys north and west of the NW Pamir massif. The extent of this glacial advance on the eastern side of the massif remains unresolved. In particular, it is unknown whether the half-graben that extends from Lake Karakul to Lake Sarez was glaciated during the Middle Pleistocene (c.f. Zabirov, 1955).
- We attribute the >100 km long Gunt valley glacier in the SW Pamir (Stübner et al., 2017) to the Bartang glacial stage. One or several Middle Pleistocene glacial advances that have been documented in the Chinese Pamir and the Muji–Tashkurgan graben system (Dabudaer and Karasu stage(s) of Seong et al., 2009; Owen et al., 2012) predate the Bartang stage.
- There is no evidence for glacial advances during the penultimate glacial cycle (MIS-6: 191–130 ky) in the western Pamir, and the Gunt and Bartang valleys may have been largely ice free. Penultimate glacial advances in the Chinese Pamir (Subakh stage of Seong et al., 2009) were less extensive than older glaciations. The oldest glacial advances documented on the Pamir plateau occurred during MIS-4 to late MIS-5 (~63–91 ky; Abramowski et al., 2006; Röhringer et al., 2012).
- After the Middle Pleistocene glacial retreat in the NW Pamir, the upper Bartang basin became clogged with voluminous debris-flow deposits, which may overlie older glacial sediments. We speculate that the abundance of silt-rich material in the alluvial sediments reflects recycling of glacial debris from the massifs north and east of the upper Bartang basin and, possibly, from the east Pamir plateau. Catastrophic mega debris flows with volumes  $\geq 0.05 \text{ km}^3$  occurred repeatedly in the basin and may reflect paraglacial destabilization of glacial deposits.
- The age of the best-dated mega debris flow ( $81 \pm 4$  ky) is similar to moraine ages ~70–80 ky documented throughout the Pamir (including the Tashkurgan valley; Abramowski et al., 2006; Röhringer et al., 2012; Owen et al., 2012; Hedrick et al., 2017). Although regional correlation of moraine ages and correlation with climate proxies is preliminary, we speculate that rising temperatures at the end of MIS-5 and/or increasing aridity due to a weakening of the mid-latitude westerlies resulted in regional glacial melting that is reflected both in the abundance of moraines of this age and in paraglacial mega debris flows.

## Author roles

Konstanze Stübner: Conceptualization; Data curation; Formal analysis; Funding acquisition; Investigation; Methodology; Project administration; Software; Validation; Visualization; Writing – original draft. Bodo Bookhagen: Methodology; Software; Validation; Data curation; Writing – review & editing. Silke Merchel: Investigation; Validation; Writing – review & editing. Johannes Lachner: Investigation; Validation; Writing – review & editing. Mustafo Gadoev: Investigation; Writing – review & editing

## Data availability

Datasets related to this article can be found at <https://github.com>.

[com/lkstueb/MoraineAge\\_GaussianMixture](https://doi.org/10.1016/j.quascirev.2021.106857).

## Declaration of competing interest

The authors declare that they have no known competing financial interests or personal relationships that could have appeared to influence the work reported in this paper.

## Acknowledgement

This study was funded by the German Science Foundation grants STU 525/2–1 and STU 525/2–2. AMS measurements at the VERA facility (Uni. Vienna) were supported by the RADIATE project under the Grant Agreement 824096319 from the EU Research and Innovation programme HORIZON 2020 via the Transnational Access grant 19001739-ST. TanDEM WorldDEM data were made accessible by the German Aerospace Center (DLR) through grant DEM\_GEOL1296. We are thankful to Jakob Heyman and an anonymous reviewer for comments and suggestions on the manuscript, to Colm O’Cofaigh for editorial handling, to Antje Musiol and Julia Artel for assistance with sample processing, and to Guillaume Dupont-Nivet and Jovid Aminov for field assistance and discussions.

## Appendix A. Supplementary data

Supplementary data to this article can be found online at <https://doi.org/10.1016/j.quascirev.2021.106857>.

## References

- Abramowski, U., Bergau, A., Seebach, D., Zech, R., Glaser, B., Sosin, P., Kubik, P.W., Zech, W., 2006. Pleistocene glaciations of Central Asia: results from  $^{10}\text{Be}$  surface exposure ages of erratic boulders from the Pamir (Tajikistan), and the Alay–Turkestan range (Kyrgyzstan). *Quat. Sci. Rev.* 25 (9–10), 1080–1096. <https://doi.org/10.1016/j.quascirev.2005.10.003>.
- Amidon, W.H., Bookhagen, B., Avouac, J.P., Smith, T., Rood, D., 2013. Late Pleistocene glacial advances in the western Tibet interior. *Earth Planet Sci. Lett.* 381, 210–221. <https://doi.org/10.1016/j.epsl.2013.08.041>.
- Applegate, P.J., Urban, N.M., Laabs, B.J.C., Keller, K., Alley, R.B., 2010. Modeling the statistical distributions of cosmogenic exposure dates from moraines. *Geosci. Model Dev. (GMD)* 3 (1), 293–307. <https://doi.org/10.5194/gmd-3-293-2010>.
- Balco, G., 2011. Contributions and unrealized potential contributions of cosmogenic-nuclide exposure dating to glacier chronology, 1990–2010. *Quat. Sci. Rev.* 30 (1–2), 3–27. <https://doi.org/10.1016/j.quascirev.2010.11.003>.
- Batbaatar, J., Gillespie, A.R., Fink, D., Matmon, A., Fujioka, T., 2018. Asynchronous glaciations in arid continental climate. *Quat. Sci. Rev.* 182, 1–19. <https://doi.org/10.1016/j.quascirev.2017.12.001>.
- Benn, D.I., Lehmkuhl, F., 2000. Mass balance and equilibrium-line altitudes of glaciers in high-mountain environments. *Quat. Int.* 65, 15–29.
- Benn, D.I., Owen, L.A., 1998. The role of the Indian summer monsoon and the mid-latitude westerlies in Himalayan glaciation: review and speculative discussion. *J. Geol. Soc.* 155 (2), 353–363. <https://doi.org/10.1144/gsjgs.155.2.0353>.
- Benn, D.I., Owen, L.A., 2002. Himalayan glacial sedimentary environments: a framework for reconstructing and dating the former extent of glaciers in high mountains. *Quat. Int.* 97, 3–25. [https://doi.org/10.1016/S1040-6182\(02\)00048-4](https://doi.org/10.1016/S1040-6182(02)00048-4).
- Borchers, B., Marrero, S., Balco, G., Caffee, M., Goehrung, B., Lifton, N., Nishizumi, K., Phillips, F., Schaefer, J., Stone, J., 2016. Geological calibration of spallation production rates in the CRONUS-Earth project. *Quat. Geochronol.* 31, 188–198. <https://doi.org/10.1016/j.quageo.2015.01.009>.
- Chevalier, M.L., Hilley, G., Tapponnier, P., Van Der Woerd, J., Liu-Zeng, J., Finkel, R.C., Ryerson, F.J., Li, H., Liu, X., 2011. Constraints on the late Quaternary glaciations in Tibet from cosmogenic exposure ages of moraine surfaces. *Quat. Sci. Rev.* 30 (5–6), 528–554.
- Clemens, S.C., Prell, W.L., 2003. A 350,000 year summer-monsoon multi-proxy stack from the Owen ridge, northern Arabian Sea. *Mar. Geol.* 201 (1–3), 35–51. <https://doi.org/10.1029/2010PA001926>.
- Derbyshire, E., 1996. Quaternary glacial sediments, glaciation style, climate and uplift in the Karakoram and northwest Himalaya: review and speculations. *Palaeogeogr. Palaeoclimatol. Palaeoecol.* 120 (1–2), 147–157. [https://doi.org/10.1016/0031-0182\(95\)00054-2](https://doi.org/10.1016/0031-0182(95)00054-2).
- Dortch, J.M., Owen, L.A., Caffee, M.W., 2010. Quaternary glaciation in the Nubra and Shyok valley confluence, northernmost Ladakh, India. *Quat. Res.* 74 (1), 132–144. <https://doi.org/10.1016/j.yqres.2010.04.013>.
- Dortch, J.M., Owen, L.A., Caffee, M.W., 2013. Timing and climatic drivers for glaciation across semi-arid western Himalayan–Tibetan orogen. *Quat. Sci. Rev.* 78, 188–208. <https://doi.org/10.1016/j.quascirev.2013.07.025>.
- Grin, E., Ehlers, T.A., Schaller, M., Sulaymonova, V., Ratschbacher, L., Gloaguen, R., 2016.  $^{10}\text{Be}$  surface-exposure age dating of the Last Glacial Maximum in the northern Pamir (Tajikistan). *Quat. Geochronol.* 34, 47–57. <https://doi.org/10.1016/j.quageo.2016.03.007>.
- Hedrick, K.A., Seong, Y.B., Owen, L.A., Caffee, M.W., Dietsch, C., 2011. Towards defining the transition in style and timing of Quaternary glaciation between the monsoon-influenced Greater Himalaya and the semi-arid Transhimalaya of Northern India. *Quat. Int.* 236 (1–2), 21–33. <https://doi.org/10.1016/j.quaint.2010.07.023>.
- Hedrick, K.A., Owen, L.A., Chen, J., Robinson, A., Yuan, Z., Yang, X., Imrecke, D.B., Li, W., Caffee, M.W., Schoenbohm, L.M., Zhang, B., 2017. Quaternary history and landscape evolution of a high-altitude intermountain basin at the western end of the Himalayan–Tibetan orogen, Waqia Valley, Chinese Pamir. *Geomorphology* 284, 156–174. <https://doi.org/10.1016/j.geomorph.2016.09.002>.
- Hewitt, K., 1999. Quaternary moraines vs catastrophic rock avalanches in the Karakoram Himalaya, northern Pakistan. *Quat. Res.* 51 (3), 220–237. <https://doi.org/10.1006/qres.1999.2033>.
- Heyman, J., Stroeven, A.P., Harbor, J.M., Caffee, M.W., 2011. Too young or too old: evaluating cosmogenic exposure dating based on an analysis of compiled boulder exposure ages. *Earth Planet Sci. Lett.* 302, 71–80. <https://doi.org/10.1016/j.epsl.2010.11.040>.
- Hijmans, R.J., Cameron, S.E., Parra, J.L., Jones, P.G., Jarvis, A., 2005. Very high resolution interpolated climate surfaces for global land areas. *Int. J. Climatol.* 25, 1965–1978. <https://doi.org/10.1002/joc.1276>.
- Korschinek, G., Bergmaier, A., Faestermann, T., Gerstmann, U.C., Knie, K., Rugel, G., Wallner, A., Dillmann, I., Dollinger, G., Lierse Von Gostomski, C., Kossett, K., 2010. A new value for the half-life of  $^{10}\text{Be}$  by heavy-ion elastic recoil detection and liquid scintillation counting. *Nucl. Instrum. Methods Phys. Res. Sect. B Beam Interact. Mater. Atoms* 268 (2), 187–191. <https://doi.org/10.1016/j.nimb.2009.09.020>.
- Lisiecki, L.E., Raymo, M.E., 2005. A Pliocene–Pleistocene stack of 57 globally distributed benthic  $\delta^{18}\text{O}$  records. *Paleoceanography* 20 (1), PA1003. <https://doi.org/10.1029/2004PA001071>.
- Marrero, S.M., Phillips, F.M., Borchers, B., Lifton, N., Aumer, R., Balco, G., 2016. Cosmogenic nuclide systematics and the CRONUScalc program. *Quat. Geochronol.* 31, 160–187. <https://doi.org/10.1016/j.quageo.2015.09.005>.
- Merchel, S., Gärtner, A., Beutner, S., Bookhagen, B., Chabilan, A., 2019. Attempts to understand potential deficiencies in chemical procedures for AMS: cleaning and dissolving quartz for  $^{10}\text{Be}$  and  $^{26}\text{Al}$  analysis. *Nucl. Instrum. Methods Phys. Res. Sect. B Beam Interact. Mater. Atoms* 455, 293–299. <https://doi.org/10.1016/j.nimb.2019.02.007>.
- Owen, L.A., Dortch, J.M., 2014. Nature and timing of Quaternary glaciation in the Himalayan–Tibetan orogen. *Quat. Sci. Rev.* 88, 14–54. <https://doi.org/10.1016/j.quascirev.2013.11.016>.
- Owen, L.A., Finkel, R.C., Caffee, M.W., Gaultier, L., 2002. Timing of multiple late Quaternary glaciations in the Hunza Valley, Karakoram Mountains, northern Pakistan: defined by cosmogenic radionuclide dating of moraines. *Geol. Soc. Am. Bull.* 114 (5), 593–604. [https://doi.org/10.1130/0013-7602\(2002\)114<0593:TOMIQLG>2.0.CO;2](https://doi.org/10.1130/0013-7602(2002)114<0593:TOMIQLG>2.0.CO;2).
- Owen, L.A., Caffee, M.W., Bovard, K.R., Finkel, R.C., Sharma, M.C., 2006. Terrestrial cosmogenic nuclide surface exposure dating of the oldest glacial successions in the Himalayan orogen: Ladakh Range, northern India. *Geol. Soc. Am. Bull.* 118 (3–4), 383–392. <https://doi.org/10.1130/B25750.1>.
- Owen, L.A., Chen, J., Hedrick, K.A., Caffee, M.W., Robinson, A.C., Schoenbohm, L.M., Yuan, Z., Li, W., Imrecke, D.B., Liu, J., 2012. Quaternary glaciation of the Tashkurgan valley, southeast Pamir. *Quat. Sci. Rev.* 47, 56–72. <https://doi.org/10.1016/j.quascirev.2012.04.027>.
- RGI Consortium, 2017. Randolph Glacier Inventory (RGI)—A Dataset of Global Glacier Outlines: Version 6.0, Technical Report, Global Land and Ice Measurements from Space. Digital Media, Boulder Colorado, USA. <https://doi.org/10.7265/N5-RGI-60>.
- Röhringer, I., Zech, R., Abramowski, U., Sosin, P., Aldahan, A., Kubik, P.W., Zöller, L., Zech, W., 2012. The late Pleistocene glaciation in the Bogchigir Valleys (Pamir, Tajikistan) based on  $^{10}\text{Be}$  surface exposure dating. *Quat. Res.* 78 (3), 590–597. <https://doi.org/10.1016/j.yqres.2012.09.002>.
- Seong, Y.B., Owen, L.A., Bishop, M.P., Bush, A., Clendon, P., Copland, L., Finkel, R., Kamp, U., Shrader Jr., J.F., 2007. Quaternary glacial history of the central Karakoram. *Quat. Sci. Rev.* 26 (25–28), 3384–3405. <https://doi.org/10.1016/j.quascirev.2007.09.015>.
- Seong, Y.B., Owen, L.A., Yi, C., Finkel, R.C., 2009. Quaternary glaciation of muztag Ata and Kongur Shan: evidence for glacier response to rapid climate changes throughout the late glacial and holocene in westernmost Tibet. *Geol. Soc. Am. Bull.* 121 (3–4), 348–365. <https://doi.org/10.1130/B26339.1>.
- Steier, P., Martschini, M., Buchriegler, J., Feige, J., Lachner, J., Merchel, S., Michlmayr, L., Priller, A., Rugel, G., Schmidt, E., Wallner, A., 2019. Comparison of methods for the detection of  $^{10}\text{Be}$  with AMS and a new approach based on a silicon nitride foil stack. *Int. J. Mass Spectrom.* 444, 116175. <https://doi.org/10.1016/j.ijms.2019.116175>.
- Stübner, K., Grin, E., Hidy, A.J., Schaller, M., Gold, R.D., Ratschbacher, L., Ehlers, T., 2017. Middle and Late Pleistocene glaciations in the southwestern Pamir and their effects on topography. *Earth Planet Sci. Lett.* 466, 181–194. <https://doi.org/10.1016/j.epsl.2017.03.012>.

- Thompson, L.O., Yao, T., Davis, M.E., Henderson, K.A., Mosley-Thompson, E., Lin, P.N., Beer, J., Synal, H.A., Cole-Dai, J., Bolzan, J.F., 1997. Tropical climate instability: the last glacial cycle from a Qinghai-Tibetan ice core. *Science* 276 (5320), 1821–1825. <https://doi.org/10.1126/science.276.5320.1821>.
- Vlasov, N.G., Dyakov, YuA., Cherev, E.S. (Eds.), 1991. *Geological Map of the Tajik SSR and Adjacent Territories, 1:500,000. Vsesozuznoi Geol. Inst., Leningrad, Saint Petersburg, Russia.*
- Von Blanckenburg, F., Hewawasam, T., Kubik, P.W., 2004. Cosmogenic nuclide evidence for low weathering and denudation in the wet, tropical highlands of Sri Lanka. *J. Geophys. Res.: Earth Surface* 109 (F3). <https://doi.org/10.1029/2003JF000049>.
- Wessel, B., Huber, M., Wohlfart, C., Marschalk, U., Kosmann, D., Roth, A., 2018. Accuracy assessment of the global TanDEM-X digital elevation model with GPS data. *ISPRS J. Photogrammetry Remote Sens.* 139, 171–182. <https://doi.org/10.1016/j.isprsjprs.2018.02.017>.
- Yao, T., Thompson, L.G., Mosbrugger, V., Zhang, F., Ma, Y., Luo, T., et al., 2012. Third pole environment (TPE). *Environmental Development* 3, 52–64. <https://doi.org/10.1016/j.envdev.2012.04.002>.
- Zabirov, R.D., 1955. *Oledenie Pamira (Pamir Glaciers)*. Geograph-GIZ Publisher, Moscow, p. 372 (in Russ.).
- Zech, R., 2012. A late Pleistocene glacial chronology from the Kitschi-Kurumdu Valley, Tien Shan (Kyrgyzstan), based on  $^{10}\text{Be}$  surface exposure dating. *Quat. Res.* 77 (2), 281–288. <https://doi.org/10.1016/j.yqres.2011.11.008>.
- Zech, R., Abramowski, U., Glaser, B., Sosin, P., Kubik, P.W., Zech, W., 2005. Late Quaternary glacial and climate history of the Pamir Mountains derived from cosmogenic  $^{10}\text{Be}$  exposure ages. *Quat. Res.* 64 (2), 212–220. <https://doi.org/10.1016/j.yqres.2005.06.002>.
- Zech, R., Röhringer, I., Sosin, P., Kabgov, H., Merchel, S., Akhmadaliev, S., Zech, W., 2013. Late Pleistocene glaciations in the Gissar Range, Tajikistan, based on  $^{10}\text{Be}$  surface exposure dating. *Palaeogeogr. Palaeoclimatol. Palaeoecol.* 369, 253–261. <https://doi.org/10.1016/j.palaeo.2012.10.031>.